Peer-reviewed version available at *Minerals* **2020**, *10*, 794; doi:10.3390/min10090794

Article

The Early Silurian Gabbro in the Eastern Kunlun Orogenic Belt, Northeast Tibet: Constraints on the Proto-Tethyan Ocean Closure

Wenxiao Zhou [1,*], Haiquan Li [1,2], Feng Chang [1,3] and Xinbiao Lv [1,4,5]

[1] Institute of Geological survey, China University of Geosciences, Wuhan 430074, China; changf@cug.edu.cn
[2] Research Institute of Petroleum Exploration & Development, Sinopec Northwest China Petroleum Bureau., Urumqi 830011, China; lhq@cug.edu.cn
[3] School of Earth and Space Sciences, Peking University, Beijing 100871, Beijing, China;
[4] Faculty of Earth Resources, China University of Geosciences, Wuhan 430074, China; lvxb_01@163.com
[5] State Key Laboratory of Geological Processes and Mineral Resources, China University of Geosciences, Wuhan 430074, China;
* Correspondence: zhouwenxiao@cug.edu.cn; Tel.: +86-0027-6788-3017

Abstract: The early Paleozoic is a crucial period in the formation and evolution of the Eastern Kunlun Orogenic Belt (EKOB), and is of great significance for understanding the evolutionary history of the Proto-Tethyan Ocean. This paper presents new petrography, geochemistry, zircon U–Pb dating, and Lu–Hf isotopic research on the Yuejingshan gabbro from the eastern segment of the EKOB. Zircon U–Pb data suggests that the gabbro formed in the Early Silurian (435 ± 2 Ma). All samples have relatively low TiO_2 contents (0.45–2.97%), widely varying MgO (6.58–8.41%) and $Mg^{\#}$ (58–65) contents, and are rich in large ion lithophile elements (LILE such as Rb, Ba, Th, and U) and light rare earth elements (LREE). This indicates that it has a similar geochemical composition to island arc basalt. The major element features indicate that the formation of this gabbro underwent fractional crystallization of clinopyroxene, olivine, and plagioclase. The depletion of high field strength elements (HFSE, such as Nb, Ta, and Ti), and a slightly positive Hf isotope (with $\varepsilon Hf_{(t)}$ ranging from 1.13 to 2.45) may be related to the partial melting of spinel-bearing peridotite, led by slab fluid metasomatism. The gabbro likely represents magmatic records of the latest period of the early Paleozoic oceanic crust subduction in the Eastern Kunlun. Therefore, the final closure of the Proto-Tethyan Ocean and the beginning of collisional orogeny occurred before the Early Silurian.

Keywords: northeast Tibet; Proto-Tethyan Ocean; early Silurian; eastern Kunlun Orogenic Belt; gabbro; zircon U–Pb dating

1. Introduction

The Eastern Kunlun Orogenic Belt (EKOB) is located in the northeast margin of the Qinghai–Tibetan Plateau, which extends for more than 1200 km and connects the Qaidam Block to the north with the Bayan Har–Songpanganzi Terrane (BH–SG) to the south [1,2]. Two significant stages of orogeny occurred in the EKOB, which are closely related to the subduction of the Proto-Tethyan Ocean during the Neoproterozoic–early Paleozoic and the Paleo-Tethyan Ocean during the Late Carboniferous–Triassic, respectively. Furthermore, these two complete tectonic cycles have established the present tectonic framework of the Eastern Kunlun region.

It is generally accepted that the Proto-Tethyan Ocean had opened and consistently expanded into the Eastern Kunlun region during the Early Cambrian; the subduction of the oceanic crust lasted until the beginning of the Early Silurian [3–6]. However, precise evidence to constrain the tectonic evolution in the Eastern Kunlun region from compression to extension during the Late Silurian is

absent. Especially, it is debated when the postcollisional extension regime was initiated. For example, Zhu and Lin [7] suggested that subduction of the oceanic crust lasted until the Early Devonian, while Dong and He [8] argued that the Proto-Tethys Ocean in the EKOB had closed and that the postcollisional extension setting occurred since the Early Devonian. Zhou and Dong [9] suggested that the postcollisional extension regime was initiated during the Late Ordovician. In contrast, Lu et al. [5] suggested that postcollisional extension was initiated at least during the Early Devonian, maybe even the Early Silurian. Therefore, it remains unclear when and how the transition from compression to extension occurred in this area.

Gabbros generally provide ample evidence, present a record of regional tectonic evolutions, and are widespread around Northeast Tibet [10]. Although an increasing number of relevant gabbros have recently been found in the center and the east of the North Kunlun Fault or the Central Kunlun Fault, their temporal role and spatial distributions as well as petrogenesis still remain obscure, which results in much contestation over the tectonic evolution of this area [11–13]. Moreover, ore bodies of magmatic sulfide deposits are found in the EKOB, such as the giant Xiarihamu Ni–Cu sulfide deposit, the large Shitoukengde Ni–Cu sulfide deposit, and the small Binggounan Ni–Cu sulfide deposit, which are hosted in olivine websterite surrounded by gabbro. Ages of the gabbroic bodies surrounding these three sulfide deposits, constrained by dating of their associated gabbros, are almost identical (Xiarihamu gabbro formed in 431 Ma, Shitoukengde gabbro formed 425 Ma, and Binggounan gabbro formed 427 Ma) [14,15]. However, there are no deposits of mining value older than 435 Ma in the EKOB. Therefore, it is essential to conduct new and accurate petrology, geochemistry, and geochronology research on gabbros of the EKOB in order to constrain the tectonic evolution of the region. This paper reports novel zircon U–Pb dating, whole rock geochemical data, and zircon Lu–Hf isotopic data for gabbros of the central EKOB. These new data provide insights to the early Paleozoic tectonic evolution of the EKOB.

2. Regional Geological Setting

As part of the Central Orogenic System of China [16–18], the EKOB is located in the northern margin of the Qinghai–Tibetan Plateau (Figure 1a). It crosses two plates of Tethyan tectonic domains: the North China Plate and the South China Plate [19]. The EKOB is located north of Bayan Kala and south of the Qaidam Basin. The western end is truncated by the Altyn Tagh strike-slip fault, while the eastern end is divided from the arc system of the Qinling by the Tangemu fault and the SaiShentang–Kuhai fault. The basic geological tectonic framework consists of several deep fault zones that strike E–W (Figure 1a) [19]. In addition to extensive magmatic activity, two ophiolite zones and three fault zones are located in the EKOB [20–22], and two ophiolite zones correspond to the Central East Kunlun Fault zone (CEKF) and the Southern East Kunlun Fault zone (SEKF). The tectonic affinities of the basement, the development of the overlying strata, and the regional tectonic evolution identify the CEKF as a brittle–ductile fracture zone with a clear surface trace and stepping geometry at depth. It separates the stable block to the north from the active block to the south. The SEKF is composed of a south-dipping thrust zone and an ophiolitic mélange zone. To date, several schemes have been proposed to divide the tectonic units of the EKOB. Although the names of these tectonic units differ, the divisions and boundaries are generally similar, mostly dividing the area into northern, central, and southern regions, which are bounded by the CEKF and the SEKF (Figure 1b) [19,23–25].

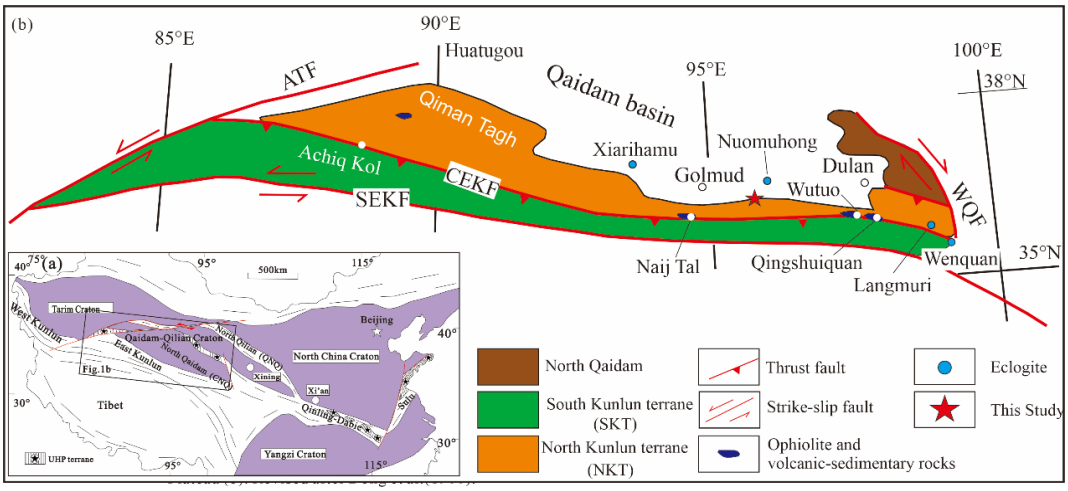

Figure 1. Geological map of the East Kunlun Orogen Belt (EKOB) and its tectonics. Abbreviations: ATF, Altyn Tagh Fault; CEKF, Central East Kunlun Fault; SEKF, Southern East Kunlun Fault; WQF, Wenquan Fault. Locations of other eclogites can be found in [26–29].

The East Kunlun consists of the North Kunlun Terrane (NKT) and the South Kunlun Terrane (SKT), which are divided by the CEKF [17,30–32]. The NKT is located between the southern margin of the Qaidam Basin and the CEKF. It is generally accepted that the EKOB experienced four orogenic cycles: Neo-Archean to Proterozoic (summarized as the Precambrian cycle by Mo [33]), the early Paleozoic cycle (the eclogite blocks that developed in the EKOB are most related to this cycle by Bian [2], Dong [8,10], and Chen [34]), the late Paleozoic–early Mesozoic cycle by Bian, Luo [23], Gu [30], and the Mesozoic to Cenozoic cycle by Gu [30], and Xu [35]. Zircon U–Pb chronology indicates that geotectonic–thermal events distribute through a wide range of 2500–1680 Ma in the source area of the Qaidam–East Kunlun basement, according to the Neo-Archean to Paleo–Proterozoic cycle [36,37]. Moreover, the crystalline basement was further solidified in the Neoproterozoic, and early magmatic activities occurred 1050–750 Ma according to geochronological data of the basalt in the lower Wanbaogou Group and Sanchakou granodiorite gneiss of the Qingshuiquan area [31]. In the process of the early Paleozoic cycle, the peripheral ocean around Qaidam experienced an important tectonic transition during which the stable Qaidam continental margin changed to an active continental margin, accompanied by extensive magmatism. Furthermore, during this cycle the tectonic evolution of the Proto–Tethys Ocean transformed from subduction–collision [31,38] to postcollision–extension. The third cycle began with the occurrence of the Late Devonian and contributed over eighty igneous rocks all over the EKOB, related to the tectonic evolution of the Paleo–Tethys Ocean [39]. After the Late Triassic, the EKOB entered the Neo-Tethys tectonic evolution stage.

The EKOB is considered to be a hard or rigid block of crystalline basement, consisting of advanced metamorphic rocks of the Paleoproterozoic Jinshuikou Group [25]. The basement is exposed on the western and southern margins of the block. The exposed strata include the Paleoproterozoic Jinshuikou Group, the Mesoproterozoic Xiaomiao Group, the Neoproterozoic QiuGuerDonggou Group, the Cambrian–early Silurian Qimantage Group, and the late Devonian Maoniushan Group. Granites are mainly Silurian–Devonian and late Permian–late Triassic in age. The SKT is located between the CEKF and the SEKF, with an E–W orientation. The block contains few intrusive rocks, including late Paleozoic–early Mesozoic granitic rocks and a small number of early Paleozoic intrusive rocks. Early Paleozoic strata are strongly deformed and were metamorphosed to granulite facies.

The Yuejinshan gabbro assumes a veinlike form, intrudes into the Jinshuikou rock group, and the boundary with the surrounding rock mostly appears as an undulating curve (Figure 2). Phenomena of contact thermal metamorphism at the boundary are obvious, and hornfelization may occasionally be found (Figure 3a). Except for the rocks at the contact boundary, which show a medium-fine grain texture (Figure 3b), all rocks in the center have a coarse grain texture (Figure 3c). Observed under a microscope, the main minerals of the rocks are plagioclase, pyroxene, and biotite.

Preprints (www.preprints.org) | NOT PEER-REVIEWED | Posted: 31 August 2020 doi:10.20944/preprints202008.0314.v2

Peer-reviewed version available at Minerals 2020, 10, 794; doi:10.3390/min10090794

Pyroxene and plagioclase have similar granularity, and are interwoven to form the gabbro texture. The pseudomorph left after pyroxene alteration and the hornblende reaction rim on the periphery of pyroxene can be seen locally (Figure 3d).

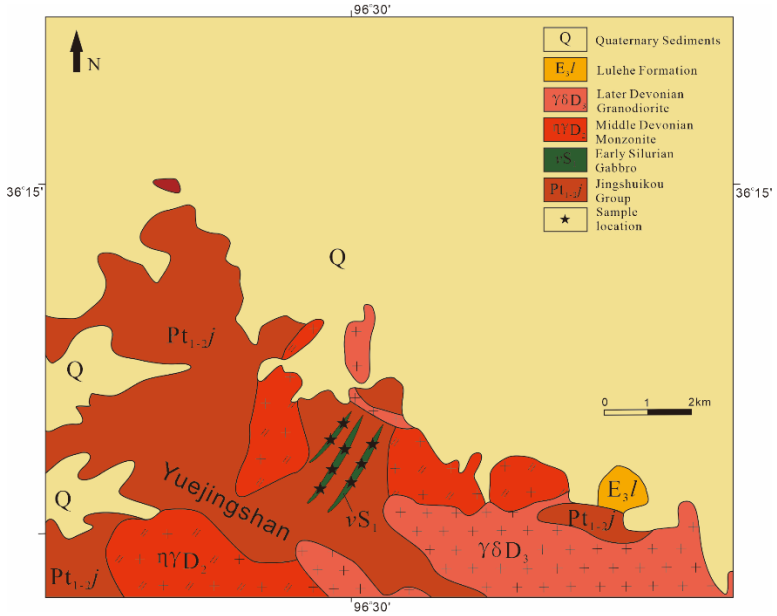

Figure 2. Simplified geological map of the Yuejingshan area.

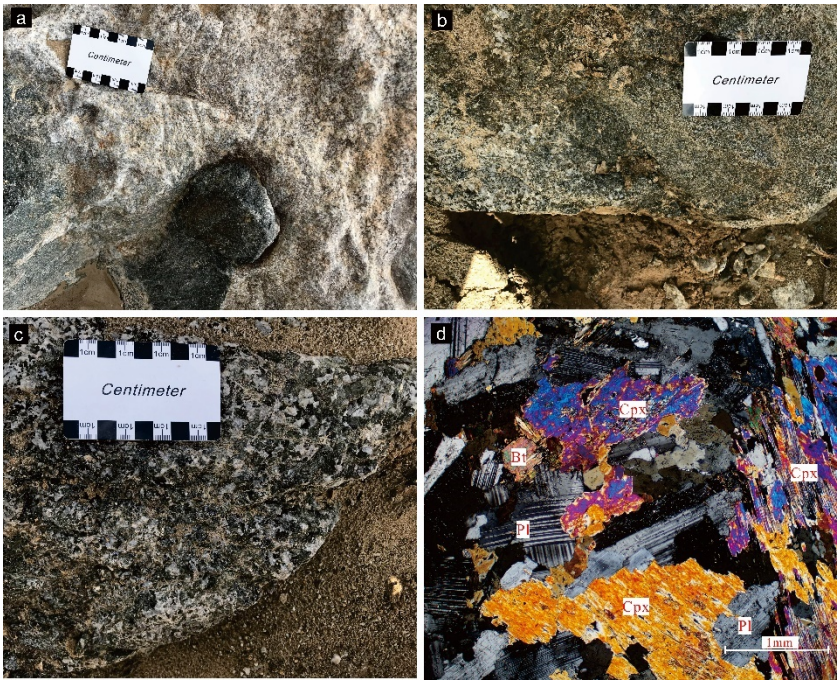

Figure 3. Outcrops and photomicrographs of Early Silurian Yuejingshan gabbro in the EKOB. (**a**) The boundary with the surrounding rock mostly follows an undulation curve. (**b**) The rocks at the contact boundary show a medium-fine grain texture. (**c**) The rocks inside have a coarse grain texture. (**d**) Photomicrograph of gabbro (cross-polarized light). Abbreviations: Cpx, clinopyroxene; Bt, biotite; Pl, plagioclase.

3. Analytical Methods

3.1. Major and Trace Elements

For geochemical analysis, after removal of altered surfaces, whole-rock samples were crushed and milled to ~75 μm. After acid digestion of samples in Teflon bombs, X-ray fluorescence (XRF; PW1401/10) with fused-glass disks and ICP–MS (Agilent 7500a with a shield torch) were used to measure the compositions of major and trace elements, respectively. These measurements were conducted at the Testing Center of Jilin University, Changchun, China. The analytical results for BHVO-1 (basalt), BCR-2 (basalt), and AGV-1 (andesite) standards indicate that the analytical precision for the detection of major elements exceeds 5%, generally exceeds 5% (~ >10 ppm) for trace elements, and is often better than 10% (~ <10 ppm). The analytical results of major and trace elements are listed in Table 2.

3.2. Zircon U–Pb Dating

Zircon crystals were extracted from whole-rock samples by a combination of magnetic and heavy liquid separation, and finally, by handpicking under a binocular microscope at the Langfang Regional Geological Survey, Hebei Province, China. All samples were examined by Olympus BX53M optical microscopy (Olympus Ltd., Tokyo, Japan), using both transmission and reflection light microscopes. To identify their internal structures, cathodoluminescence (CL) images were obtained by a JEOL scanning electron microscope (JEOL Ltd., Tokyo, Japan). Grains of transparent, euhedral, unfractured, and inclusion-free zircons were chosen for isotopic analysis. Zircon U–Pb dating and trace element analysis were conducted by Sample Solution Analysis Laboratories Ltd. The analysis used a beam diameter of 30 μm and an ablation depth of 20–40 μm. Helium was used as carrier gas to transport the ablated material from the standard laser-ablation cell. Zircon 91500 was used as the external standard for age calibration [40], and Nist 610 and GJ-1 were used as external standards to calculate concentrations [41]. ^{29}Si was used as the internal standard element. Analytical methods are available in the literature [42]. Laser sampling was performed using a GeolasPro laser ablation system that consists of a COMPexPro 102 ArF excimer laser (wavelength of 193 nm and maximum energy of 200 mJ) and a MicroLas optical system (MicroLas Ltd., Frankfurt, Germany). An Agilent Technologies Ltd. (Santa Clara, CA, USA) 7700e ICP–MS instrument was used to acquire ion-signal intensities. Helium was applied as carrier gas. Argon was used as make-up gas and mixed with the carrier gas via T-connector before entering the ICP. This laser ablation system includes a "wire" signal smoothing device [43]. The spot size and frequency of the laser were set to 32 μm and 5 Hz, respectively. Common Pb was corrected using the method proposed by Andersen [44]. The ICP–MS–DATECAL program was used to calculate isotopic ratios and element contents [45,46]. The age calculations and Concordia plots were made using Isoplot version 4.15 [47] and listed Table 2.

3.3. Zircon Hf Isotopic Analysis

Zircon Hf isotopic analysis was conducted using a NewWave UP213 LA–MC–ICP–MS at the Institute of Mineral Resources, Chinese Academy of Geological Sciences, Beijing, China. The instrument conditions and data acquisition methods followed Wu et al. [48]. During Hf isotope analysis, a laser repetition rate of 7 Hz was used, and the spot size was 45 μm. The original counting rates of ^{172}Yb, ^{173}Yb, ^{175}Lu, ^{176} (Hf + Yb + Lu), ^{177}Hf, ^{178}Hf, ^{179}Hf, ^{180}HF, and ^{182}W were collected, and the isobaric interference correction of ^{176}Hu and ^{176}Yb on ^{176}HF was determined. The zircon Hf isotopic data obtained in this study are presented in Table 3.

Preprints (www.preprints.org) | NOT PEER-REVIEWED | Posted: 31 August 2020 doi:10.20944/preprints202008.0314.v2

Peer-reviewed version available at Minerals 2020, 10, 794; doi:10.3390/min10090794

4. Analytical Results

4.1. Whole-Rock Geochemistry

The test results for the major and trace elements of the whole rock and the related parameters are listed in Table 1. Diagrams related to the main, rare earth, and trace elements are all drawn using GEOKIT software [49].

The Yuejingshan gabbros have low SiO_2 (48.05–55.56 wt.%), MgO (6.58–8.41 wt.%), total Fe_2O_3 (2.87–3.39 wt.%), total alkali (ALK 0.73–3.51 wt.%), and high Al_2O_3 (13. 95–16.73 wt.%) contents (Table 1). On a total alkali vs. silica (TAS) classification diagram, according to Middlemost [50], the plot falls into the gabbro field (Figure 4a). Geochemically, the Yuejingshan gabbros belong to subalkaline series with calc-alkaline affinity (Figure 4b,c,d). Their ratios of aluminum to calcium+natrium+kalium (A/CNK) are 0.57–0.72, showing peraluminous characteristics ($(K_2O + Na_2O) < Al_2O_3 < (CaO + K_2O + Na_2O)$).

On a primitive mantle (PM)-normalized trace element spider diagram (Figure 5b), the samples show enrichment in light rare earth elements (LREEs) and large ion lithophile elements (LILEs; e.g., Sr, Rb, Ba, U, and K), while being depleted in heavy rare earth elements (HREEs) and high field strength elements (HFSEs; e.g., Nb, Ta, Ti, and P) (Figure 5a). They have $(La/Yb)_N$ ratios of 2.66–5.77 and Eu/Eu^* values of 0.23–1.91.

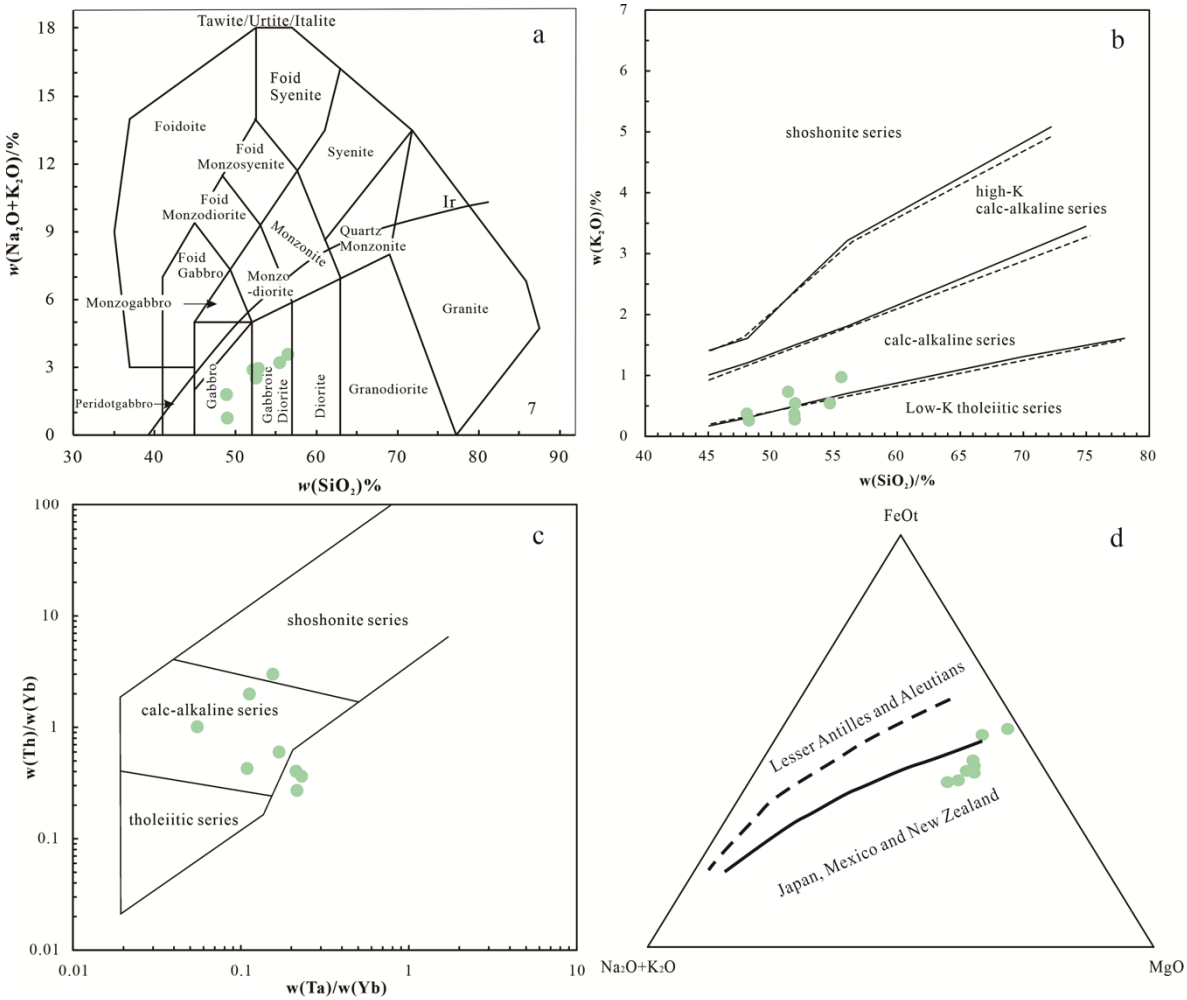

Figure 4. Total alkali vs. silica (TAS) diagrams (**a**), modified from Middlemost [50]; K_2O vs. SiO_2 (**b**), modified from Winchester and Floyd [51]; Th/Yb vs. Ta/Yb (**c**), modified from Pearce [52]; and Total alkali - Total FeOt- MgO (AFM) classification diagrams (**d**) after Coleman [53] for Yuejingshan gabbro samples.

Table 1. Major (wt.%) and trace element (ppm) data for Yuejingshan gabbro.

Peer-reviewed version available at Minerals 2020, 10, 794; doi:10.3390/min10090794

Samples	YJHC-1	YJHC-2	YJHC-3	YJHC-4	YJHC-5	YJHC-6	YJHC-7	YJHC-8
SiO_2	51.86	51.88	48.05	51.83	54.64	48.21	55.56	51.33
TiO_2	0.53	0.53	5.50	0.51	0.45	2.97	0.53	1.60
Al_2O_3	16.44	16.73	3.02	16.56	16.21	13.95	15.86	15.18
Fe_2O_3	0.81	1.16	1.40	1.02	0.84	1.28	0.85	0.71
FeO	7.52	6.58	12.82	6.87	6.00	9.40	5.82	7.43
MnO	0.15	0.13	0.26	0.14	0.11	0.18	0.11	0.14
MgO	7.72	7.55	12.07	7.67	6.99	8.43	6.58	8.41
CaO	10.93	10.72	13.98	11.29	9.93	11.92	9.32	10.65
Na_2O	2.18	2.33	0.35	2.11	2.60	1.49	2.53	2.08
K_2O	0.28	0.55	0.38	0.37	0.55	0.27	0.98	0.73
P_2O_5	0.05	0.03	0.06	0.03	0.03	0.10	0.04	0.05
LOI	0.89	1.16	0.47	0.92	0.96	0.52	1.14	1.04
Total	99.35	99.35	98.34	99.33	99.31	98.72	99.33	99.34
A/NK	4.23	3.79	3.10	4.29	3.33	5.10	3.04	3.60
A/CNK	0.69	0.70	0.11	0.68	0.71	0.57	0.72	0.64
A/MF	0.53	0.56	0.06	0.54	0.59	0.38	0.61	0.46
C/MF	0.64	0.65	0.50	0.67	0.66	0.60	0.65	0.59
$Mg^{\#}$	62.52	63.84	60.45	63.71	64.84	58.73	64.04	65.02
Rb	10.75	21.47	20.20	15.68	22.83	11.17	48.78	37.99
Ba	127.33	177.01	208.33	121.93	152.28	175.39	215.03	223.13
Th	0.53	0.50	3.96	0.77	6.42	0.81	8.03	0.97
U	0.24	0.26	0.82	0.36	1.29	0.31	1.22	0.28
Nb	1.31	1.74	1.98	1.30	2.36	5.11	2.51	2.82
Ta	0.335	0.393	0.214	0.196	0.36	0.423	0.412	0.271
Ce	11.83	16.30	21.82	16.39	32.93	17.82	38.06	19.01
Sr	339.44	315.80	38.14	298.41	303.63	276.16	275.61	281.30
Nd	7.72	10.91	19.08	10.73	21.25	12.12	22.71	11.97
P	196.00	144.00	240.00	144.00	144.00	436.00	192.00	196.00
Zr	20.40	21.24	52.08	23.22	36.00	31.21	51.98	22.09
Hf	0.90	1.35	1.17	1.17	1.35	0.99	1.62	0.81
Ti	3201.00	3189.00	32,961.00	3063.00	2692.00	17,793.00	3177.00	9610.00
La	5.40	8.31	7.64	7.84	12.87	8.41	21.38	9.22
Ce	11.83	16.30	21.82	16.39	32.93	17.82	38.06	19.01
Pr	1.71	2.56	3.93	2.51	4.94	2.79	5.83	2.87
Nd	7.72	10.91	19.08	10.73	21.25	12.12	22.71	11.97
Sm	2.11	2.82	5.98	2.81	5.48	3.19	5.01	2.87
Eu	1.33	1.41	0.46	1.31	1.43	1.23	1.43	1.30
Gd	2.16	2.81	6.20	2.86	5.19	3.29	4.37	2.74
Tb	0.39	0.49	1.16	0.51	0.93	0.56	0.77	0.47
Dy	2.59	3.40	7.77	3.39	6.04	3.70	4.76	3.16
Ho	0.56	0.69	1.61	0.71	1.29	0.79	1.01	0.66
Er	1.56	1.93	4.34	1.96	3.58	2.16	2.77	1.80
Tm	0.23	0.29	0.64	0.29	0.52	0.31	0.42	0.28
Yb	1.46	1.82	3.90	1.80	3.20	1.99	2.66	1.61
Lu	0.24	0.28	0.64	0.29	0.49	0.30	0.43	0.26
Y	12.34	15.55	34.98	15.41	29.51	17.00	22.74	14.66
ΣREE	39.28	54.03	85.16	53.40	100.14	58.65	111.60	58.21
LREE	30.11	42.31	58.92	41.59	78.90	45.56	94.41	47.24
HREE	9.17	11.72	26.25	11.81	21.24	13.10	17.19	10.97
LREE/HREE	3.28	3.61	2.24	3.52	3.72	3.48	5.49	4.31
La_N/Yb_N	2.66	3.27	1.41	3.12	2.88	3.04	5.77	4.11
δEu	1.91	1.53	0.23	1.42	0.82	1.16	0.94	1.42
δCe	0.95	0.87	0.98	0.91	1.01	0.90	0.84	0.91
Nb/La	0.24	0.21	0.26	0.17	0.18	0.61	0.12	0.31
Nb/Ce	0.11	0.11	0.09	0.08	0.07	0.29	0.07	0.15
Nb/Ta	3.90	4.42	9.26	6.61	6.56	12.08	6.09	10.42
Zr/Hf	22.66	15.74	44.51	19.84	26.67	31.52	32.09	27.27
Ce/Y	0.96	1.05	0.62	1.06	1.12	1.05	1.67	1.30
Tb_N/Yb_N	1.22	1.22	1.35	1.28	1.32	1.29	1.31	1.33
Th/Yb	0.36	0.27	1.02	0.43	2.00	0.41	3.02	0.60
Th/Nb	0.41	0.29	2.00	0.60	2.72	0.16	3.20	0.34
Ba/Th	239.80	356.16	52.58	157.53	23.73	217.61	26.79	229.79
Ba/La	23.58	21.31	27.26	15.56	11.83	20.85	10.06	24.21
Sr/Nd	43.96	28.96	2.00	27.82	14.29	22.78	12.14	23.50

Preprints (www.preprints.org) | NOT PEER-REVIEWED | Posted: 31 August 2020 doi:10.20944/preprints202008.0314.v2

Peer-reviewed version available at Minerals 2020, 10, 794; doi:10.3390/min10090794

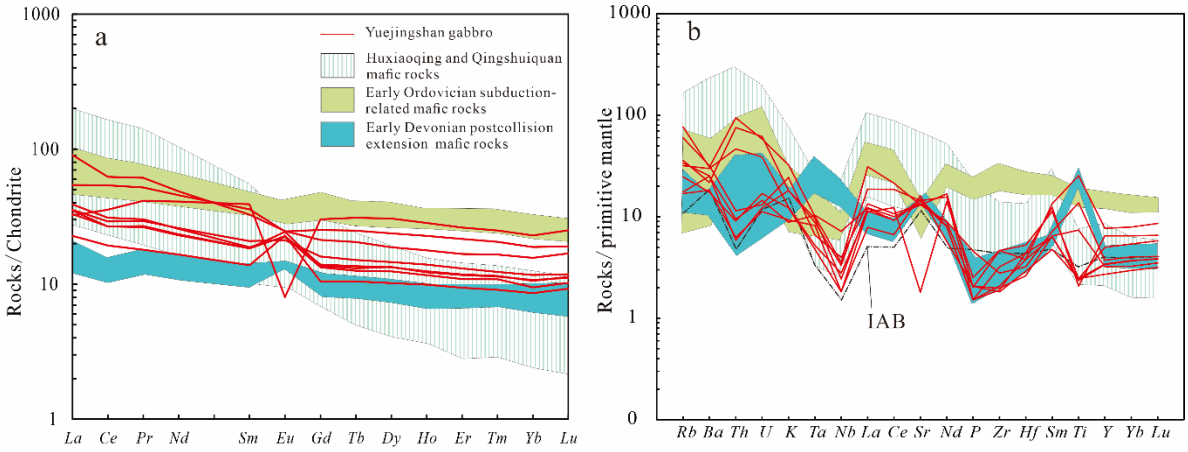

Figure 5. Chondrite-normalized rare-earth element distribution patterns (**a**) normalization values modified from Taylor and McLennan [54]) and primitive mantle-normalized trace element spider diagrams; (**b**) normalization values modified from Sun and McDonough [55] of Yuejinshan gabbro samples. Island arc basalt (IAB) data are from Niu and O'Hara [56]; data of early Ordovician subduction-related mafic rocks are from Cui, Meng [38]; data of Huxiaoqing mafic rocks are from Liu, Ma [10]; data of Early Devonian postcollision extension mafic rocks are from Liu, Ma [57].

4.2. Zircon U–Pb Ages

Zircon U–Pb age results are presented in Table 2 and Figure 6a. Zircons from the Yuejingshan gabbro (YJHC-1) are mostly colorless to pale brown, euhedral, or subhedral crystals (100–200 μm long) with aspect ratios of 1:1–2:1. Most zircons display clear oscillatory zoning and annulus zoning, while a number of grains display convoluted, disrupted zoning and rim overgrowths (Figure 7). These features, together with increased Th/U ratios (most exceed 0.4; see Table 2), indicate a magmatic origin [58–61]. The $^{206}Pb/^{238}U$ ages of 27 analytical spots range from 428 to 443 Ma, yielding a weighted mean $^{206}Pb/^{238}U$ age of 435 ± 2 Ma [Mean Standard Weighted Deviation (MSWD) = 0.03, Figure 6b].

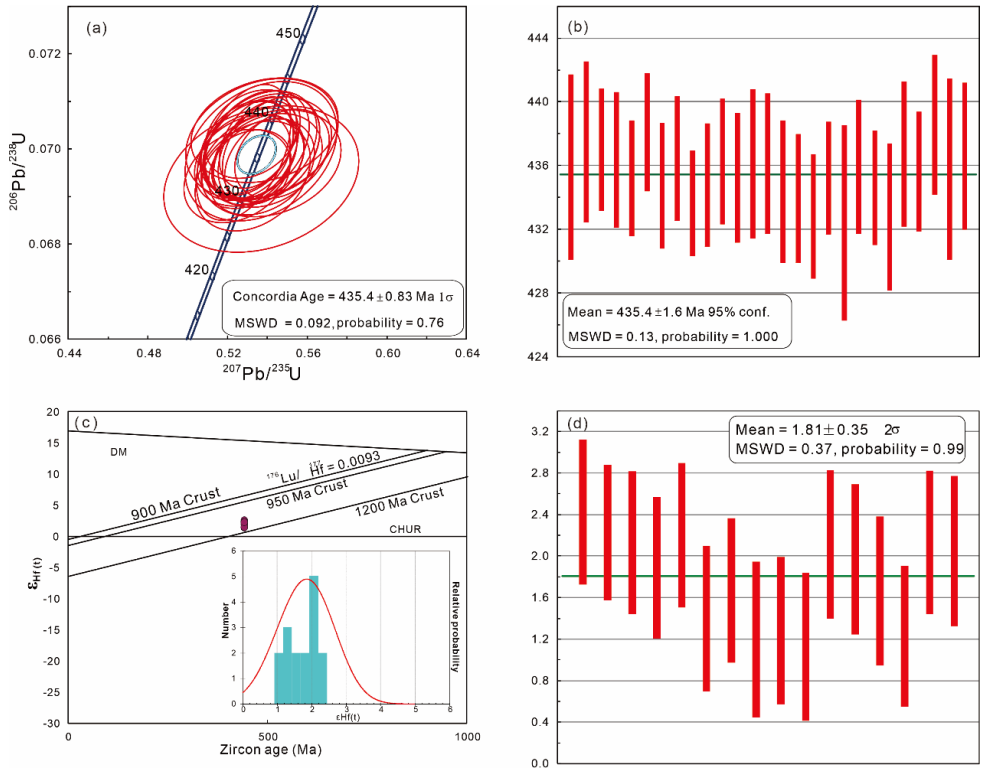

Figure 6. (**a**) for U–Pb concordia diagrams: (**b**) weighted average ages; (**c**) $\varepsilon Hf_{(t)}$ crust evolution diagrams, and (**d**) weighted average $\varepsilon Hf_{(t)}$ values of Yuejingshan gabbro samples. Mean for weighted average ages; MSWD for Mean Standard Weighted Deviation.

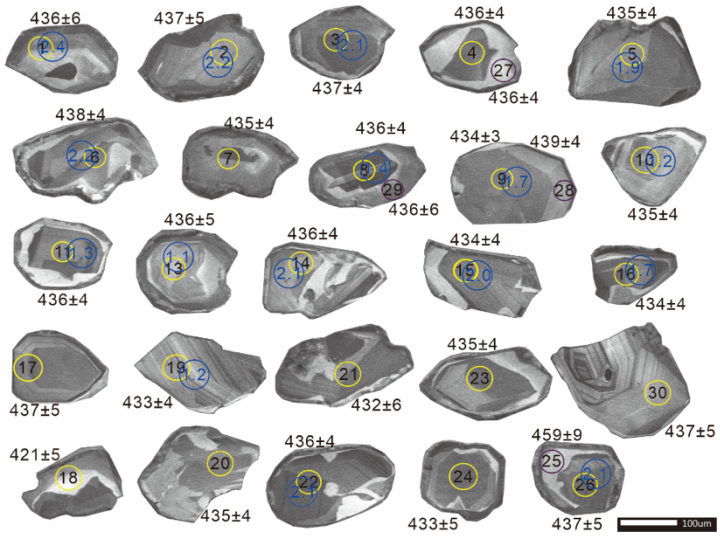

Figure 7. Zircon cathodoluminescence (CL) images of Yuejingshan gabbro. Yellow circles and black numbers represent U–Pb test spots and ages. Blue circles and numbers represent Lu–Hf tested spots and related $\varepsilon Hf_{(t)}$ values.

Table 2. LA–ICP–MS zircon U–Pb isotopic ratios and apparent ages of the zircons from Yuejingshan gabbro.

Spots	^{207}Pb[a]	Pb_{Total}	Th[b]	U[b]	Th/U[b]	$^{206}Pb^{c}/^{238}U$		$^{207}Pb^{c}/^{235}U$		$^{207}Pb^{c}/^{206}Pb$		Rho[d]	$^{206}Pb/^{238}U$		$^{207}Pb/^{235}U$		$^{207}Pb/^{206}Pb$		Concordance
	CPS	ppm	ppm	ppm		Ratio	±1σ[e]	Ratio	±1σ	Ratio	±1σ		(Ma)	±1σ	(Ma)	±1σ	(Ma)	±1σ	
YJHC-01	408	40.08	98.55	348.39	0.28	0.06995	0.00097	0.53688	0.02512	0.05648	0.00284	0.29	436	6	436	17	472	111	99%
YJHC-02	606	78.74	257.21	598.01	0.43	0.07021	0.00084	0.53725	0.02523	0.05551	0.00263	0.25	437	5	437	17	432	138	99%
YJHC-03	1158	158.01	542.83	1147.79	0.47	0.07013	0.00064	0.53527	0.01285	0.05546	0.00141	0.38	437	4	435	8	432	57	99%
YJHC-04	990	153.51	527.52	1108.62	0.48	0.07003	0.00071	0.53945	0.02169	0.05585	0.00236	0.25	436	4	438	14	456	94	99%
YJHC-05	732	94.78	299.35	751.13	0.40	0.06983	0.00060	0.52819	0.01539	0.05497	0.00165	0.30	435	4	431	10	409	67	98%
YJHC-06	969	158.14	595.48	1086.29	0.55	0.07032	0.00061	0.53256	0.01581	0.05491	0.00163	0.29	438	4	434	10	409	67	98%
YJHC-07	835	108.34	366.80	814.08	0.45	0.06976	0.00065	0.53979	0.01836	0.05604	0.00188	0.27	435	4	438	12	454	76	99%
YJHC-08	2030	193.34	616.88	1449.99	0.43	0.07004	0.00065	0.52956	0.01553	0.05485	0.00165	0.31	436	4	432	10	406	64	98%
YJHC-09	640	101.87	356.30	716.72	0.50	0.06957	0.00054	0.52949	0.01466	0.05528	0.00153	0.28	434	3	431	10	433	61	99%
YJHC-10	726	98.36	279.09	813.10	0.34	0.06976	0.00064	0.53090	0.01815	0.05511	0.00188	0.27	435	4	432	12	417	81	99%
YJHC-11	908	127.84	430.74	978.27	0.44	0.07001	0.00065	0.53026	0.01491	0.05482	0.00147	0.33	436	4	432	10	406	61	99%
YJHC-12	957	117.23	365.82	958.46	0.38	0.06984	0.00067	0.53403	0.01385	0.05557	0.00144	0.37	435	4	434	9	435	62	99%
YJHC-13	558	69.64	239.59	540.61	0.44	0.06999	0.00077	0.53710	0.01932	0.05548	0.00189	0.31	436	5	437	13	432	76	99%
YJHC-14	845	97.76	320.63	751.68	0.43	0.06999	0.00073	0.54189	0.01610	0.05609	0.00161	0.35	436	4	440	11	457	63	99%
YJHC-15	1030	104.98	323.36	843.41	0.38	0.06970	0.00074	0.54178	0.02323	0.05614	0.00233	0.25	434	4	440	15	457	91	98%
YJHC-16	1066	123.13	370.94	996.53	0.37	0.06963	0.00066	0.53716	0.01748	0.05579	0.00186	0.29	434	4	437	12	443	74	99%
YJHC-19	713	73.90	229.30	596.73	0.38	0.06943	0.00065	0.52479	0.01757	0.05462	0.00180	0.28	433	4	428	12	398	79	98%
YJHC-20	1025	136.49	501.54	945.67	0.53	0.06984	0.00058	0.53371	0.01392	0.05514	0.00143	0.32	435	4	434	9	417	55	99%
YJHC-21	1082	106.30	362.70	809.95	0.45	0.06937	0.00102	0.53699	0.03234	0.05564	0.00332	0.24	432	6	436	21	439	133	99%
YJHC-22	1728	224.52	816.17	1616.77	0.50	0.06996	0.00070	0.53550	0.01332	0.05509	0.00131	0.40	436	4	435	9	417	58	99%
YJHC-23	1257	147.01	538.22	1064.23	0.51	0.06974	0.00060	0.53854	0.01328	0.05578	0.00139	0.35	435	4	437	9	443	56	99%
YJHC-24	768	94.57	343.30	704.55	0.49	0.06944	0.00076	0.53265	0.01908	0.05546	0.00203	0.31	433	5	434	13	432	81	99%
YJHC-26	957	130.27	484.79	925.38	0.52	0.07009	0.00075	0.53486	0.01730	0.05508	0.00181	0.33	437	5	435	11	417	74	99%
YJHC-27	713	102.17	332.99	767.02	0.43	0.06990	0.00062	0.54729	0.01570	0.05644	0.00164	0.31	436	4	443	10	478	32	98%
YJHC-28	724	89.70	284.45	713.62	0.40	0.07039	0.00073	0.53858	0.02444	0.05523	0.00247	0.23	439	4	437	16	420	98	99%
YJHC-29	1229	113.98	238.54	1078.95	0.22	0.06993	0.00094	0.52801	0.01563	0.05447	0.00157	0.45	436	6	430	10	391	65	98%
YJHC-30	691	77.84	253.85	627.90	0.40	0.07007	0.00076	0.53650	0.01875	0.05523	0.00193	0.31	437	5	436	12	420	78	99%

[a]Within-run background-corrected mean ^{207}Pb signal in counts per second. [b]U and Pb content and Th/U ratio were calculated relative to GJ-1 and are accurate to approximately 10%. [c]Corrected for background, mass bias, laser-induced U–Pb fractionation and common Pb (if detectable, see analytical method) using Stacey and Kramers [62] model Pb composition. $^{207}Pb/^{235}U$ calculated using $^{207}Pb/^{206}Pb/(^{238}U/^{206}Pb \times 1/137.88)$. Errors are propagated by quadratic addition of within-run errors (2SE) and the reproducibility of GJ-1 (2SD). [d]Rho is the error correlation defined as $err^{206}Pb/^{238}U/err^{207}Pb/^{235}U$. [e]**All results are tested and calculated under 1σ.**

Table 3. LA–MC–ICP–MS zircon Lu–Hf isotope data for the zircons from Yuejingshan gabbro.

Spots	$^{176}Hf/^{177}Hf$	1σ	$^{176}Lu/^{177}Hf$	1σ	$^{176}Yb/^{177}Hf$	1σ	Age (Ma)	$^{176}Hf/^{177}Hf$ (t)	$\varepsilon_{Hf}(t)$	1σ	T_{DM1}	T_{DM2}	$f_{Lu/Hf}$
YJHC-01	0.282575	0.000012	0.000586	0.000005	0.019114	0.000230	436	0.282570	2.451123	0.698450	0.95	1.16	–0.98
YJHC-02	0.282568	0.000010	0.000358	0.000008	0.011535	0.000245	437	0.282565	2.275424	0.651632	0.95	1.17	–0.99
YJHC-03	0.282566	0.000012	0.000507	0.000004	0.016676	0.000101	437	0.282562	2.177404	0.685086	0.96	1.17	–0.98
YJHC-04	0.282561	0.000012	0.000791	0.000001	0.026815	0.000096	436	0.282555	1.910605	0.681251	0.97	1.19	–0.98
YJHC-05	0.282568	0.000012	0.000562	0.000001	0.017963	0.000088	435	0.282564	2.204613	0.693689	0.96	1.17	–0.98
YJHC-06	0.282545	0.000012	0.000529	0.000020	0.017255	0.000715	438	0.282541	1.467534	0.700865	0.99	1.21	–0.98
YJHC-07	0.282554	0.000012	0.000582	0.000003	0.019450	0.000128	435	0.282549	1.671190	0.695060	0.98	1.20	–0.98
YJHC-08	0.282541	0.000014	0.000697	0.000013	0.022012	0.000405	436	0.282536	1.223624	0.748791	1.00	1.23	–0.98

YJHC-09	0.282546	0.000013	0.001035	0.000029	0.034477	0.001021	434	0.282538	1.265352	0.706653	1.00	1.22	–0.97
YJHC-10	0.282539	0.000013	0.000660	0.000003	0.020823	0.000166	435	0.282534	1.131614	0.712386	1.00	1.23	–0.98
YJHC-11	0.282566	0.000013	0.000594	0.000002	0.018700	0.000092	436	0.282561	2.137195	0.714768	0.96	1.18	–0.98
YJHC-12	0.282561	0.000014	0.000443	0.000001	0.014240	0.000057	435	0.282557	1.974358	0.723604	0.96	1.18	–0.99
YJHC-13	0.282554	0.000013	0.000711	0.000007	0.023546	0.000257	436	0.282549	1.688117	0.718018	0.98	1.20	–0.98
YJHC-14	0.282541	0.000011	0.000516	0.000006	0.016402	0.000217	436	0.282536	1.255510	0.676370	0.99	1.22	–0.98
YJHC-15	0.282565	0.000012	0.000433	0.000004	0.013554	0.000178	434	0.282562	2.115202	0.687449	0.96	1.17	–0.99
YJHC-16	0.282567	0.000013	0.000908	0.000002	0.029073	0.000104	434	0.282560	2.031208	0.721509	0.97	1.18	–0.97

4.3. Zircon Lu–Hf Isotopic Compositions

The results of Hf isotope analysis are presented in Table 3 and Figure 6c. The spot locations on the zircon grains are indicated with blue circles in Figure 7. All tested spots showed a low ratio of $^{176}Lu/^{177}Hf$ (0.000358–0.001035, Table 3), which indicates no significant radioactivity. Hf accumulated after zircon had formed. The measured $^{176}Hf/^{177}Hf$ ratio may represent the composition for the zircons forming stage [63]. The $^{176}Hf/^{177}Hf$ ratios of 16 measuring spots are relatively concentrated and distributed in the range 0.282534–0.282570. The $\varepsilon Hf_{(t)}$ values are positive, ranging from 1.13 to 2.45 (with an average of 1.81, Figure 6d). In addition, the 16-point two-stage model ages (T_{DM2}) range from 1.16 to 1.23 Ga, which is much older than the crystallization age (435 ± 2 Ma). This indicates an origin from the enriched mantle source area or contamination by crustal materials during the magmatic evolution process. This composition suggests Ordovician–Silurian reworking of a Mesoproterozoic juvenile crust. The Neoproterozoic globular granitic gneiss in the vicinity of these gabbros in the Nomuhong area also proved to have originated from Mesoproterozoic ancient crustal material [64].

5. Discussion

5.1. Fractional Crystallization and Crustal Contamination

The contents of $Mg^{\#}$, Cr, and Ni in the Yuejinshan gabbro samples float slightly. The contents of $Mg^{\#}$ range from 58 to 65, those of Cr from 89 to 157 ppm, and those of Ni from 13.0 to 25 ppm. These characteristics indicate that it is not obvious that fractional crystallization of this gabbro occurred before the final emplacement. The binary diagram, with $Mg^{\#}$ as abscissa, shows that only Cr and Ni are very weakly positively correlated with $Mg^{\#}$ (Figure 8), indicating that fractional crystallization of clinopyroxene and olivine did not occur or is not obvious in the formation of the magma [65–67]. P_2O_5, FeO_T, and TiO_2 exhibit significant negative correlations with $Mg^{\#}$, indicating that the magma possibly experienced fractional crystallization of apatite and iron–titanium oxide. The ratio $(2CaO + Na_2O)/TiO_2$ shows clear negative correlation with Al_2O_3/TiO_2 (Figure 9), and part of the samples display an obvious Eu negative anomaly. This suggests that the magma underwent fractional crystallization of plagioclase [68]. In summary, the Yuejinshan gabbros magma likely experienced mainly fractional crystallization of apatite, iron, titanium oxide, and plagioclase during its formation.

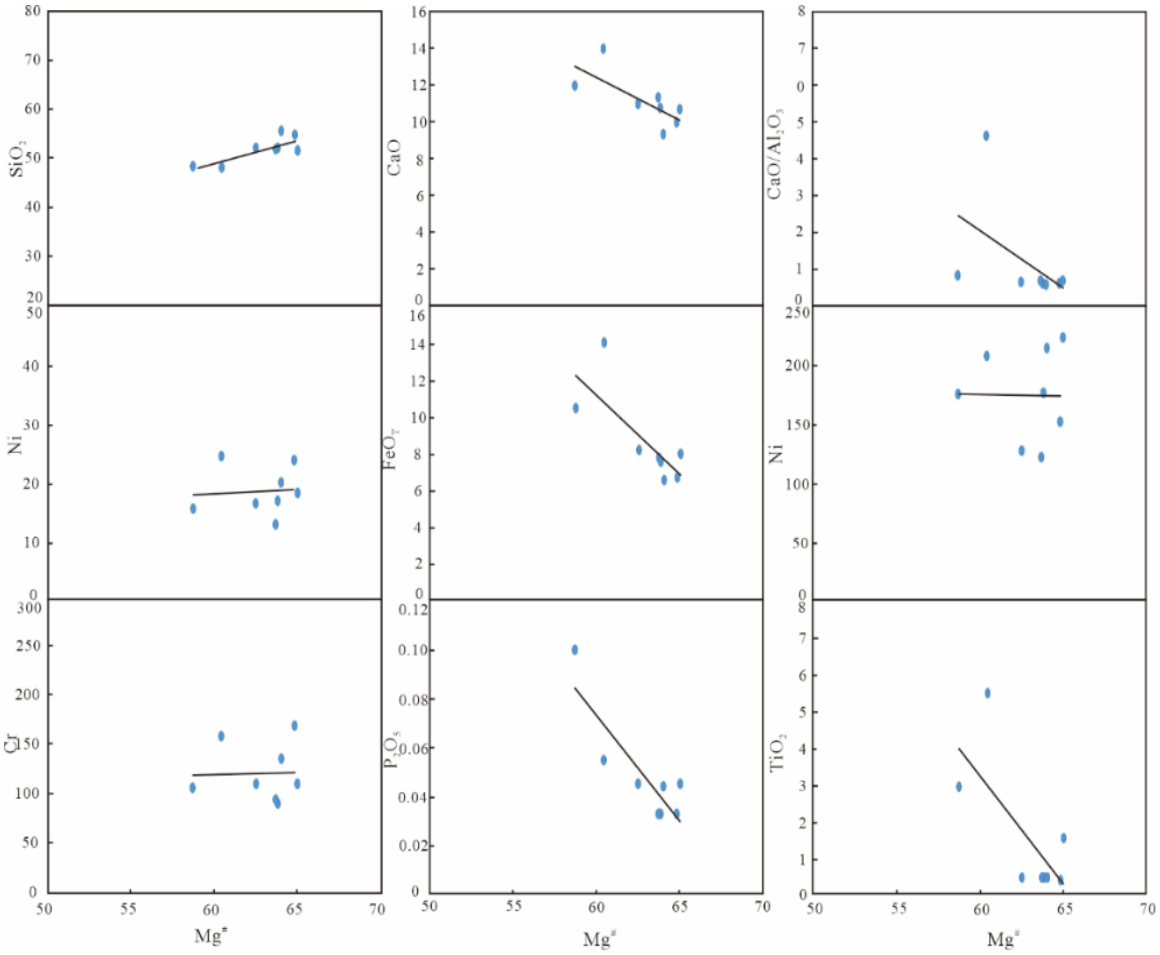

Figure 8. Variation diagrams of SiO_2, TiO_2, FeO_T, CaO, P_2O_5, Cr, Ni, CaO/Al_2O_3, and Sc/Y versus $Mg^{\#}$ for Yuejingshan gabbro samples.

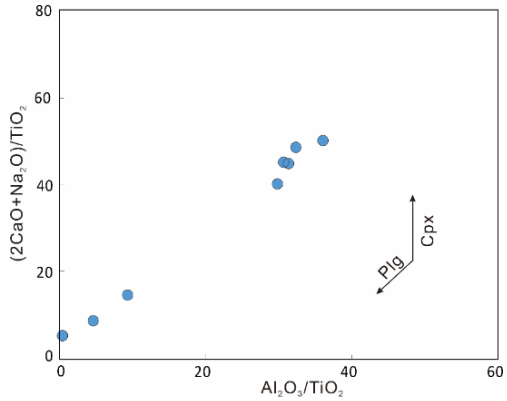

Figure 9. Diagram of $(2CaO + Na_2O)/TiO_2$ versus Al_2O_3/TiO_2 of Yuejingshan gabbro samples (modified form Dessureau et al. [68]).

Studies have shown that crustal contamination and fractional crystallization often occur simultaneously in the process of magmatic evolution and emplacement [69–71]. Crustal contamination commonly increases LILE, K_2O, and Na_2O, while decreasing P_2O_5 and TiO_2 [71,72]. The binary diagram, constructed with $Mg^{\#}$ as the abscissa, shows that as $Mg^{\#}$ decreases, P_2O_5 and TiO_2 gradually increase (Figure 8). This is inconsistent with the characteristics of mafic magma, formed under the involvement of crustal contamination. The Yuejinshan gabbros have relatively lower Nb/La and Nb/Ce ratios (ranging from 0.12 to 0.31 and from 0.07 to 0.29, respectively), which are lower than the Nb/La and Nb/Ce ratios of the primitive mantle, the average crust, and the average lower crust (1.02, 0.4; 0.69, 0.33; and 0.83, 0.39, respectively) [54]. This suggests that mafic magma

may not form by mixing a certain proportion of crustal and mantle material. In addition, a few inherited zircon cores in the CL image analysis and slightly positive $\varepsilon Hf_{(t)}$ values (1.13–2.45) were found in the gabbros, indicating that a small amount of crustal contamination occurred once. Therefore, it may be concluded that the Yuejinshan gabbros were contaminated to a lesser extent by the crust during their formation process.

5.2. Nature of the Mantle Source

Mafic rocks, e.g., gabbro, usually derive from the lithospheric mantle or asthenospheric mantle [72,73]. Compared with the primitive mantle, rocks derived from the lithospheric mantle are generally enriched in LILE and LREE and depleted in HFSE (e.g., Nb, Ta, and Ti). However, materials from the asthenospheric mantle are normally enriched in LILE and HFSE and possess isotopic compositions characterized by the depleted mantle. The gabbro samples from Yuejinshan all have relatively low TiO_2 (ranging from 0.45% to 2.97%), are rich in LILE (i.e., Rb, Ba, Th, and U), and show obvious depletion of HFSE (i.e., Nb, Ta, and Ti) compared with the primitive mantle (Figure 5b). Moreover, they show a slightly positive Hf isotope composition ($\varepsilon Hf_{(t)}$ values between 1.13 and 2.45); Hf-t_{DM} (in scope from 0.95 to 1.00 Ga) is much earlier than its crystallization age (~435 Ma), indicating that the gabbros are a product of reworked Mesoproterozoic (1.16–1.23 Ga) juvenile crust of the lithospheric mantle. The Yuejinshan gabbros have a relatively low Ce/Y ratio (ranging from 0.62 to 1.67, with an average value of 1.10), indicating that it may derive from the spinel–garnet facies-stable area with a depth ranging from 60 to 80 km [74]. The low $(Tb/Yb)_N$ ratio (ranging from 1.22 to 1.35, with an average of 1.29) of the rocks further confirms that the mafic rocks were derived from the partial melting of spinel-bearing peridotite [75].

Compared with Huxiaoqing mafic rocks, Yuejinshan gabbro samples have a relatively lower Th/Yb ratio (ranging from 0.27 to 2.00). The points plotted in Th/Yb–Nb/Yb diagrams all deviate clearly from the MORB–OIB evolution line (Figure 10), suggesting that its formation is significantly affected by the subduction component [76]. The transformation of the mantle source area through plate subduction is mainly realized through interaction between fluid or melt derived from altered oceanic crust or subduction zone sediments and mantle peridotite [77–79]. Mafic magma ultimately formed by the interaction between mantle peridotite and slab melt, which generally contains relatively high Na_2O, P_2O_5, and TiO_2 levels, and shows positive anomalies of the elements Nb, Ta, and Ti compared with the primitive mantle [77,80]. The Yuejinshan gabbro samples have lower TiO_2 and P_2O_5 contents, and show obvious negative anomalies of elements Nb, Ta, and Ti compared with the primitive mantle. Basically, the interaction between mantle peridotite and slab fluid can be excluded. Trace element ratios (Ba/Th, Th/Nb, Ba/La, and Th/Yb) may identify hydrous fluid or subduction zone sediments. All Yuejinshan gabbro samples have relatively concentrated Th/Nb and Th/Yb ratios (in the ranges of 0.29–3.20 and 0.27–3.02, respectively), and a wider variation range of Ba/Th and Ba/La ratios (in the ranges of 23.73–356.16 and 10.06–27.26, respectively) (Figure 11). These data imply that a large amount of hydrous fluid entered the mantle source area [78,79,81]. Moreover, most rock samples have a wider variation range of Sr/Nd ratios and relatively stable Th/Yb ratios (in the ranges of 2.00–43.96 and 0.27–3.02, respectively), suggesting that the hydrous fluid mainly originated from the altered oceanic crust [82].

Preprints (www.preprints.org) | NOT PEER-REVIEWED | Posted: 31 August 2020 doi:10.20944/preprints202008.0314.v2

Peer-reviewed version available at Minerals 2020, 10, 794; doi:10.3390/min10090794

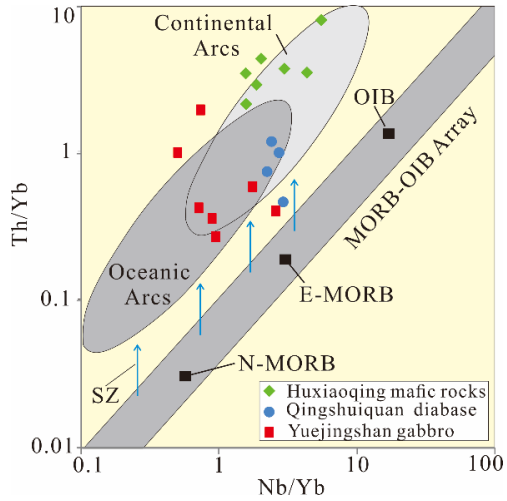

Figure 10. Th/Yb versus Nb/Yb diagram for Yuejingshan gabbro samples (modified from Pearce [83]). Data of Huxiaoqing mafic rocks originate from Liu, Ma [10]; data of Early Devonian postcollision extension mafic rocks originate from Liu, Ma [57].

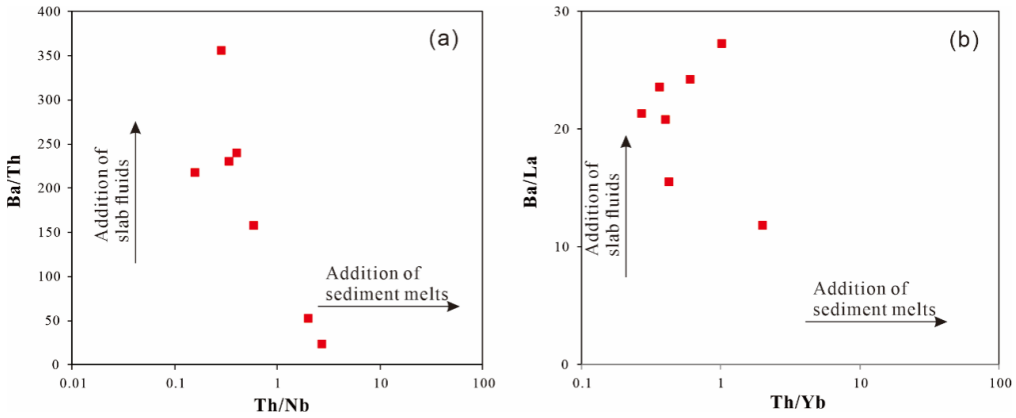

Figure 11. Ba/Th vs. Th/Nb (**a**) modified from Hanyu, Tatsumi [78]) and Ba/La vs. Th/Yb; (**b**) modified from Woodhead et al. [81]) diagrams for Yuejingshan gabbro samples.

In summary, it may be concluded that the genesis of Yuejinshan gabbros is related to the partial melting of spinel-bearing peridotite replaced by slab hydrous fluid. Moreover, their formation underwent fractional crystallization of clinopyroxene, olivine, and plagioclase.

5.3. Implications for the Early Silurian Tectonic Nature of the EKOB

Compared with the primitive mantle, Yuejinshan gabbro samples are rich in LILE (e.g., Rb, Ba, Th, and U) and LREE, but are clearly depleted in HFSE (e.g., Nb, Ta, and Ti). These characteristics are similar to the features of island arc basalt and the Early Ordovician Eastern Kunlun mafic rocks with island arc characteristics (Figure 12). However, they obviously differ from the mafic rocks related to the postcollision extension during the Early Devonian in Eastern Kunlun (Figure 5), indicating that it is closely related to subduction. Based on the studies of Qingshuiquan, Kekesha, and Nuomuhong ophiolites from the Early Cambrian to the Early Ordovician, the existence of an early Paleozoic ocean was identified [3,84,85] (Figure 13a). Many high-temperature peraluminous–strong peraluminous granites (the saturation temperatures of most zircons exceed 800 °C), magnesium-rich diorite ($Mg^{\#}$ all exceed 45), and a small number of HFSE-enriched gabbros (such as Nb, Ta, and Ti) were identified to belong to the age from the Late Silurian to the Early Devonian [10,57,86,87]. This indicates that the East Kunlun region had begun postcollision extension during this period. However, there is still much controversy over the final closure of the early Paleozoic ocean basin in East Kunlun and when collision orogeny began. Mo et al. [33] suggested that the emergence of Late Ordovician amphibole schist and its associated gabbro (Ar–Ar age is 445 ± 2 Ma)

Peer-reviewed version available at *Minerals* **2020**, *10*, 794; doi:10.3390/min10090794

in the southwest of Tumuluk, Qimantag, could be regarded as a sign of the end of subduction and the beginning of collision. However, Ren et al. [88] and Gao et al. [89] considered that in the Late Ordovician–Early Silurian, the oceanic basin had still not been closed, the East Kunlun region was in a stage of partial back arc extension, and the final closing time of the ocean basin was in the Middle Silurian [34]. The findings on Wanbaogou rapakivi granite reported by Wang et al. [90] suggested that the continental collision had ended and had entered the postorogenic extensional stage during the Late Ordovician. The Yuejinshan gabbros reported in this paper may provide crucial petrologic evidence for further investigation of the specific tectonic evolution history of the East Kunlun region from the Late Ordovician to the Early Silurian. This evidence may be used to determine the conversion time between the oceanic crust subduction and collision orogeny during the early Paleozoic in the East Kunlun region.

Moreover, previous analysis on its petrogenesis also confirmed that the subduction components (especially from hydrous fluid) contributed more to the mantle source area. These characteristics suggest that the Yuejinshan gabbros most likely formed in a subduction-related environment. However, two studies have also shown that mafic rocks, which formed during the postcollision extension period, tend to have a similar geochemical composition to island arc basalt because they inherited mantle source areas modified by paleoslab subduction [91,92] (Figure 13b). The crystallization age of Yuejinshan gabbros belongs to the Early Silurian (435 ± 2 Ma), which is clearly earlier than the metamorphic age (428 Ma) of the collision-related eclogite facies [26] and the peak metamorphic age (427 Ma) [34] of medium pressure (epidotization) amphibolite facies in the EKOB. This indicates that it could not have formed during the postcollision extensional stage. Ren et al. [88] and Liu et al. [10] reported that Qingshuiquan diabase (438 ± 1 Ma) and Huxiaoqin mafic rocks (438 ± 2 Ma), respectively, also possess Early Silurian subduction magmatic characteristics and are situated in the middle Kunlun suture zone. Both are similar to the Yuejinshan gabbros reported in this paper in terms of age, spatial distribution, and geochemical composition (Figures 1 and 10). These similarities indicate that these three sets of mafic rocks could have formed in an identical tectonic setting.

Subduction-related intrusive rocks with ages of 515–436 Ma (e.g., Qingshuiquan, Kekesha, and Huxiaoqing) are found in the Northern and Middle Kunlun Areas. These include calc-alkaline gabbro, diabase, diorite, quartz diorite, and granodiorite, which have been reported in the southern part of the Qingshuiquan–Nuomuhong ophiolites [10,88,93,94]. Additionally, granulite with a metamorphic age of 508 ± 8 Ma, as well as gneisses and amphibolites with ages of 517–482 Ma have been reported, thus confirming the connections of the tectonic thermal events to oceanic crust subduction [95,96].

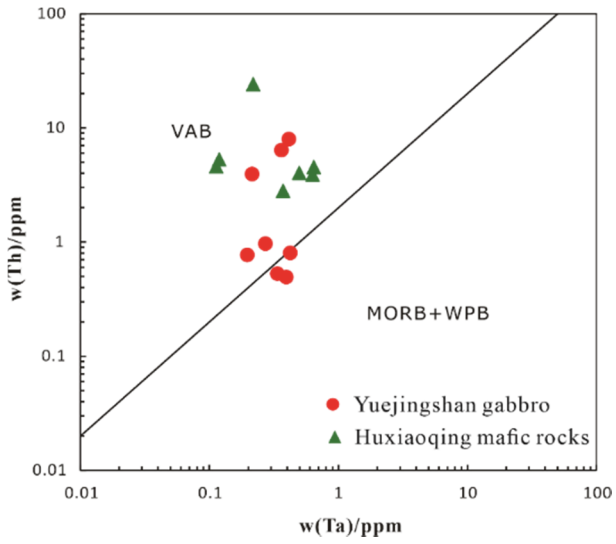

Figure 12. Th vs. Ta diagram for Yuejingshan gabbro samples. Data for Huxiaoqing mafic rocks originate from Liu, Ma [10].

In addition, based on the existing regional data, it can be inferred that the magmatic rocks between 515 and 436 Ma are dominated by diorite, basalt, andesite, and gabbro with island arc magmatic rocks [3,84,85]. However, the magmatic rocks between 430 Ma and 391 Ma are mainly A-type granites, peraluminous–strong peraluminous granites [57], magnesia-rich diorite, and gabbro (Figure 13c). The magmatic rocks of the two periods are obviously different, which may correspond to oceanic crust subduction and postcollision, respectively, indicating extension of two different tectonic evolution processes. All previous research implied that the ocean during the early Paleozoic opened at least at the early Cambrian and the subduction lasted from the Ordovician to the early Silurian [35,96,97].

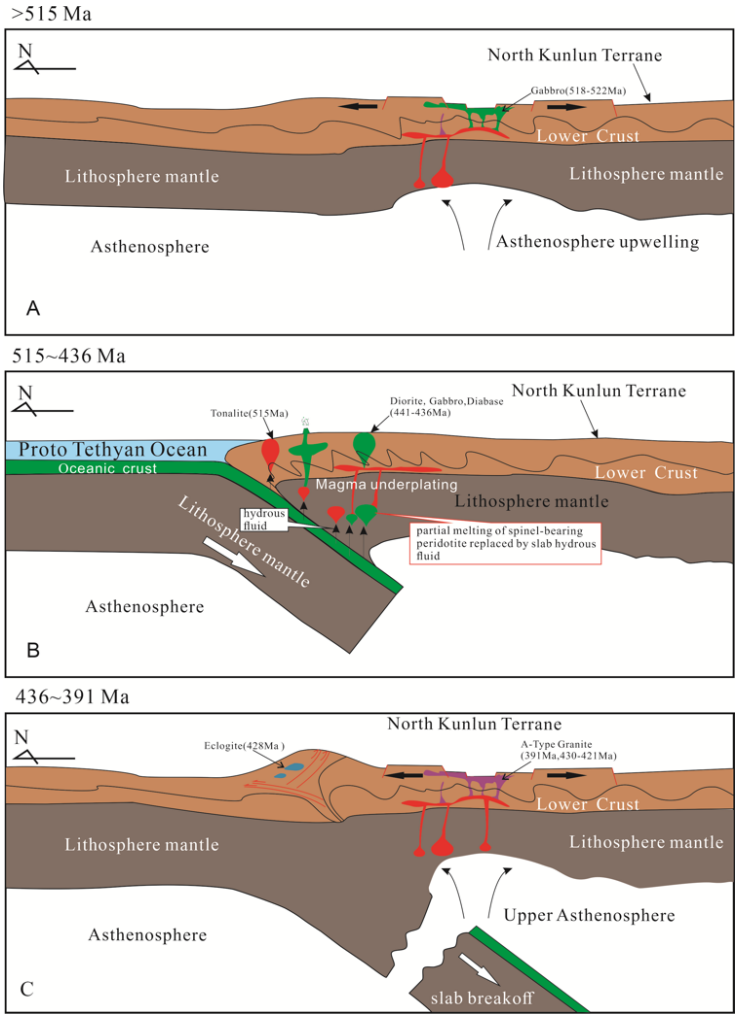

Figure 13. Summary of early Paleozoic magmatic, metamorphic, and tectonic evolution of the Eastern Kunlun Orogen. a, from the Early Cambrian to the Early Ordovician, the existence of an early Paleozoic ocean was identified; b, two studies [91,92] have also shown that mafic rocks, which formed during the postcollision extension period, tend to have a similar geochemical composition to island arc basalt because they inherited mantle source areas modified by paleoslab subduction; c, the magmatic rocks between 430 Ma and 391 Ma are mainly A-type granites, peraluminous–strong peraluminous granites [57], magnesia-rich diorite, and gabbro. Data originate from the literature [1,14,15].

6. Conclusions

(1) LA–ICP–MS zircon U–Pb dating showed the age of the Yuejingshan gabbros at ~435 Ma.

(2) Yuejingshan gabbro formed from the partially melting of spinel-bearing peridotite interpreted by plate fluid, and was subjected to fractional crystallization of olivine, plagioclase, and clinopyroxene.

Peer-reviewed version available at *Minerals* **2020**, *10*, 794; doi:10.3390/min10090794

(3) The geochronology and geochemical characteristics of the Yuejingshan gabbros indicate that the EKOB was in a postcollisional extensional environment during the Early Silurian, which was triggered by slab break-off.

(4) The gabbro reflects the magmatic record of the latest period of the early Paleozoic oceanic crust subduction in the Eastern Kunlun. The region witnessed the final closure of the Proto-Tethyan Ocean and the beginning of collisional orogeny, which occurred before the Early Silurian.

Supplementary Materials: The following are available online at www.mdpi.com/xxx/s1: Table S1: Major (wt.%) and trace element (ppm) data for Yuejingshan gabbro, Table S2: LA–ICP–MS zircon U–Pb isotopic ratios and apparent ages of zircons of the Yuejingshan gabbro, Table S3: LA–MC–ICP–MS zircon Lu–Hf isotope data for the zircons from Yuejingshan gabbro.

Author Contributions: Conceptualization, W.Z.; Data curation, W.Z. and H.L.; Formal analysis, W.Z. and F.C.; Project administration, W.Z. and X.L.; Resources, W.Z. and X.L.; Writing—original draft, W.Z.; Writing—review and editing, W.Z. and X.L.

Funding: This study was supported by the National Natural Science Foundation of China (No. 41703024) and the work items of the China Geological Survey (No. 12120114018001).

Acknowledgments: We would like to thank Yuan Yu from the State key laboratory of geological processes and mineral resources of China University of Geosciences for his support and assistance on zircon U–Pb and Hf isotope calculating. We acknowledge the help of Xia Bin, Mao Cheng, and Zhao Xiaocheng, who participated in the field work. The authors are grateful for the critical comments from two anonymous reviewers, which profoundly enhanced the quality of this manuscript.

Conflicts of Interest: The authors declare no conflict of interest.

References

1. Chen, N.; Sun, M.; Wang, Q.; Zhao, G.; Chen, Q.; Shu, G. EMP chemical ages of monazites from Central Zone of the eastern Kunlun Orogen: Records of multi-tectonometamorphic events. *Chin. Sci. Bull.* **2007**, *52*, 2252–2263.
2. Bian, Q.T.; Li, D.H.; Pospelov, I.; Yin, L.M.; Li, H.S.; Zhao, D.S.; Chang, C.F.; Luo, X.Q.; Gao, S.L.; Astrakhantsev, O.; et al. Age, geochemistry and tectonic setting of Buqingshan ophiolites, North Qinghai-Tibet Plateau, China. *J. Asian Earth Sci.* **2004**, *23*, 577–596.
3. Yang, J.S.; Robinson, P.; Jiang, C.F.; Xu, Z.Q. Ophiolites of the Kunlun Mountains, China and their tectonic implications. *Tectonophysics* **1996**, *258*, 215–231.
4. Lu, N.S.; Yu, H.F.; Zhao, F.Q. *Precambrian Geology in Northern Tibetan Plateau*; Geological Publishing House: Beijing, China, 2002.
5. Lu, L., Zhang, Y., Wu, Z. and Hu, D. Zircon U-Pb dating of Early Paleozoic granites from the East Kunlun Mountains and its geological significance. *Acta Geosci. Sin*. **2013**, *34*, 447–454.
6. Zhang, J.Y.; Ma, C.Q.; Xiong, F.H.; Liu, B. Petrogenesis and tectonic significance of the Late Permian–Middle Triassic calc-alkaline granites in the Balong region, eastern Kunlun Orogen, China. *Geol. Mag.* **2012**, *149*, 892–908.
7. Zhu, Y.; Lin, Q.; Jia, C.; Wang, G. SHRIMP zircon U-Pb age and significance of Early Paleozoic volcanic rocks in East Kunlun orogenic belt, Qinghai Province, China. *Sci. China Ser. D Earth Sci.* **2006**, *49*, 88–96.
8. Dong, Y.; He, D.; Sun, S.; Liu, X.; Zhou, X.; Zhang, F.; Yang, Z.; Cheng, B.; Zhao, G.; Li, J. Subduction and accretionary tectonics of the East Kunlun orogen, western segment of the Central China Orogenic System. *Earth Sci. Rev.* **2018**, *186*, 231–261.
9. Zhou, B.; Dong, Y.; Zhang, F.; Yang, Z.; Sun, S.; He, D. Geochemistry and zircon U-Pb geochronology of granitoids in the East Kunlun Orogenic Belt, northern Tibetan Plateau: Origin and tectonic implications. *J. Asian Earth Sci.* **2016**, *130*, 265–281.
10. Liu, B., Ma, C., Jiang, H., Guo, P., Zhang, J. and Xiong, F. Early Paleozoic tectonic transition from ocean subduction to collisional orogeny in the Eastern Kunlun region: Evidence from Huxiaoqin mafic rocks. *Acta Petrol. Sin*. **2013**, *29*, 2093–2106.
11. Hao, N.N., Yuan, W.M., Zhang, A.K., Cao, J.H., Chen, X.N., Feng, Y.L. and Li, X. Late Silurian to Early Devonian granitoids in the Qimantage Area, East Kunlun Mountains: LA-ICPMS zircon U–Pb ages, geochemical features and geological setting. *Geol. Rev.* **2014**, *60*, 201–215.

12. Li, B.L., Sun, F.Y., Yu, X.F., Qian, Y., Wang, G. and Yang, Y.Q. U-Pb dating and geochemistry of diorite in the eastern section from eastern Kunlun middle uplifted basement and granitic belt. *Acta Petrol. Sin.* **2012**, *28*, 1163–1172.
13. Lu, L., Wu, Z., Hu, D., Barosh, P.J., Hao, S. and Zhou, C. Zircon U-Pb age for rhyolite of the Maoniushan Formation and its tectonic significance in the East Kunlun Mountains. *Acta Petrol. Sin*. **2010**, *26*, 1150–1158.
14. Du, W., Jiang, C., Ling, J., Zhou , W., Xia, M. and Xia, Z. Zircon SHRIMP U-Pb geochronology, geochemistry and implications of No.II intrusion in Xiarihamu Cu-Ni deposit, East Kunlun Mountains. *Miner. Depos.* **2017**, *36*, 1185–1196.
15. Zhang, Z., Wang, C., Qian, B. and Li, W. The geochemistry characteristics of Silurian gabbro in East Kunlun Orogenic Belt and its mineralization relationship with magmatic Ni-Cu sulfide deposit. *Acta Petrol. Sin.* **2018**, *34*, 2262–2274.
16. Pan, G.T., Li, X.Z., Wang, L.Q., Ding, J. and Chen, Z.L. Preliminary division of tectonic nits of the Qinghai-Tibet Plateau and its adjacent regions. *Geol. Bull. China* **2002**, *21*, 701–707.
17. Xu, Z.Q., Yang, J.S., Li, H.B., Zhang, J.X., Zeng, L.S. and Jiang, M. The Qinghai-Tibet plateau and continental dynamics: A review on terrain tectonics, collisional orogenesis, and processes and mechanisms for the rise of plateau. *Geol. China* **2006**, *33*, 221–238.
18. Yin, F.H.; Zhang, K.X. Characteristics of the easrern Kunlun orogenic belt. *Earth Sci.* **1997**, *22*, 339–342.
19. Fan, L.K.; et al. Characters and Evolution of the Geodynamics in the East Kunlun. *Geol. Surv. Res*. **2009**, *32*, 181–186.
20. Shen, Y.C., Yang, J.Z., Liu, T.B., Li, G.M. and Zeng, Q.D. The discovery of ophioite in the Qimantha area, East Kunlun, Xinjiang, China. *Geol. Rev.* **2000**, *46*, 92.
21. Zhu, Y.H., Zhang, K.X., Yuan, P., Chen, N.S., Wang, G.C. and Hou, G.J. Determination of different ophiolitic belts in eastern Kunlun orogenic zone and their tectonic significance. *Earth Sci. J. China Univ. Geosci.* **1999**, *24*, 134–138.
22. Qi, X.P., Yang, J., Fan, X.G., Cui, J.T., Cai, Z.F., Zeng, X.W., Wei, W., Qu, X.X. and Zhai, Y.M. Age, geochemical characteristics and tectonic significance of Changshishan ophiolite in central East Kunlun tectonic mélange belt along the east section of East Kunlun Mountains. *Geol. China* **2016**, *43*, 797–816.
23. Bian, Q.T., Luo, X.Q., Li, H.S. and Zhao, D.S. Discovery of Early Paleozoic and Early Carboniferous-Early Permian ophiolites in the Animaqing, Qinghai, China. *Sci. Geol. Sin*. **1999**. *34*, 523–524.
24. Gao, L.Y.; Wu, X.N.; Zuo, G.C. *The Characters and Tectonic Significance of Ophiolite First Discovered in Qinshuiquan Area, East Kunlun*; Chinese Academy of Geological Sciences, Xi'an Institute of Geology and Mineral Resources: Xi'an, China, 1988.
25. Jiang, C.F., Yang, J.S., Feng, B.G., Zhu, Z.Z., Zhao, M., Chai, Y.C., Shi, X.D., Wang, H.D. and Hu, J.Q. *Opening-Closing Tectonics of Kunlun Mountains*; Geological Publishing House: Beijing, China, 1992.
26. Meng, F.; Zhang, J.; Cui, M. Discovery of Early Paleozoic eclogite from the East Kunlun, Western China and its tectonic significance. *Gondwana Res.* **2013**, *23*, 825–836.
27. Meng, F.C., Cui, M.H., Jia, L.H., Ren, Y.F. and Feng, H.B. Paleozoic continental collision of the East Kunlun orogen: Evidence from protoliths of the eclogites. *Acta Petrol. Sin*. **2015**, *31*, 3581–3594.
28. Qi, S.S., Song, S.G., Shi, L.C., Cai, H.J. and Hu, J.C. Discovery and its geological significance of Early Paleozoic eclogite in Xiarihamu-Suhaitu area, western part of the East Kunlun. *Acta Petrol. Sin*. **2014**, *30*, 3345–3356.
29. Qi, X.P., Fan, X.G., Yang, J., Cui, J.T., Wang, B.Y. and Fan, Y.Z. The discovery of Early Paleozoic eclogite in the upper reaches of Langmuri in eastern East Kunlun Mountains and its significance. *Geol. Bull. China* **2016**, *35*, 1771–1783.
30. Gu, F.B. Geological characteristics of East Kunlun and tectonic evolution in late Paleozic-Mesozoic Era. *Geol. Qinghai* **1994**, *1*, 4–14.
31. Li, H.K., Lu, S.N., Xiang, Z.Q., Zhou, H.Y., Guo, H., Song, B., Zheng, J.K. and Gu, Y. SHRIMP U-Pb zircon age of the granulate from the Qingshuiquan area, Central Eastern Kunlun Suture Zone. *Earth Sci. Front.* **2006**, *13*, 311–321.
32. Wu, J.G.; Xiao, X.C.; Li, T.D. The Yadong-Golmud geoscience section on the Qinghai-Tibet Plateau. *Acta Geol. Sin*. **1989**, *63*, 285–296.
33. Mo, X.X., Luo, Z.H., Deng, J.F., Yu, X.H., Liu, C.D., Chen, H.W. and Liu, H.Y. Granitoids and Crustal Crowth in the East Kunlun Orogenic Belt. *Geol. J. China Univ.* **2007**, *13*, 403–414.
34. Chen, N. Precise timing of the Early Paleozoic metamorphism and thrust deformation in the Eastern Kunlun Orogen. *Chin. Sci. Bull.* **2002**, *47*, 1130.

35. Xu, W.L.; Wang, Q.H.; Wang, D.Y.; Guo, J.H.; Pei, F.P. Mesozoic adakitic rocks from the Xuzhou–Suzhou area, eastern China: Evidence for partial melting of delaminated lower continental crust. *J. Asian Earth Sci.* **2006**, *27*, 230–240.
36. Chen, Y.X., Pei, X.Z., Li, R.B., Liu, Z.Q., Li, Z.C., Zhang, X.F., Chen, G.C., Liu, Z.G., Ding, S.P. and Guo, J.F. Zircon U-Pb Age of Xiaomiao Formation of Proterozoic in the Eastern Section of the East Kunlun Orogenic Belt. *Geoscience* **2011**, *25*, 510–521.
37. Wang, G.C., Wei, Q.R., Jia, X.Y., Zhang, K.X., Li, D.W., Zhu, Y.H. and Xiang, S.Y. Some ideas of Precambrian Geology in the East Kunlun, China. *Geol. Bull China* **2007**, *26*, 929–937.
38. Cui, H.M.; Meng, F.C.; Wu, X.K. Early Ordovician island arc of Yaziquan, west of Qimantag Mountain, East Kunlun: Evidences from geochemistry, Sm-Nd isotope and geochronology of intermediate-basic rocks. *Acta Petrol. Sin.* **2011**, *27*, 3365–3379.
39. Feng, C.Y., Wang, X.P., Shu, X.F., Zhang, A.K., Ye, X., Liu, J.N., MA, S.C., Li, G.C. and LI, D.X. Isotopic Chronology of the Hutouya Skarn Lead-Zinc Polymetailic Ore District in Qimantage Area of Qinghai Province and Its Geological Significance. *J. Jilin* **2011**, *41*, 1806–1817.
40. Wiedenbeck, M.; Allé, P.; Corfu, F.; Griffin, W.L.; Meier, M.; Oberli, F.; Von Quadt, A.; Roddick, J.; Spiegel, W. Three natural zircon standards for the U-Th-Pb, Lu-Hf, trace element and ree analyses. *Geostand. Geoanal. Res.* **1995**, *19*, 1–23.
41. Jackson, S.E.; Pearson, N.J.; Griffin, W.L.; Belousova, E.A. The application of laser ablation-inductively coupled plasma-mass spectrometry to in situ U–Pb zircon geochronology. *Chem. Geol.* **2004**, *211*, 47–69.
42. Yuan, H.; Gao, S.; Liu, X.; Li, H.; Günther, D.; Wu, F. Accurate U-Pb Age and Trace Element Determinations of Zircon by Laser Ablation-Inductively Coupled Plasma-Mass Spectrometry. *Geostand. Geoanal. Res.* **2004**, *28*, 353–370.
43. Hu, Z.; Zhang, W.; Liu, Y.; Gao, S.; Li, M.; Zong, K.; Chen, H.; Hu, S. "Wave" Signal-Smoothing and Mercury-Removing Device for Laser Ablation Quadrupole and Multiple Collector ICPMS Analysis: Application to Lead Isotope Analysis. *Anal. Chem.* **2014**, *87*, 1152–1157.
44. Andersen, T. Correction of common lead in U–Pb analyses that do not report 204Pb. *Chem. Geol.* **2002**, *192*, 59–79.
45. Liu, Y.; Gao, S.; Hu, Z.; Gao, C.; Zong, K.; Wang, D. Continental and Oceanic Crust Recycling-induced Melt-Peridotite Interactions in the Trans-North China Orogen: U-Pb Dating, Hf Isotopes and Trace Elements in Zircons from Mantle Xenoliths. *J. Pet.* **2009**, *51*, 537–571.
46. Liu, Y.; Hu, Z.; Gao, S.; Günther, D.; Xu, J.; Gao, C.; Chen, H. In situ analysis of major and trace elements of anhydrous minerals by LA-ICP-MS without applying an internal standard. *Chem. Geol.* **2008**, *257*, 34–43.
47. Ludwig, K.R. Isoplot 3.00: *A Geochronological Toolkit for Microsoft Excel*; Berkeley Geochronology Center Special Publication; BGC: Berkeley, CA, USA, 2003; Volume 4, p. 70.
48. Wu, F.; Yang, Y.-H.; Xie, L.-W.; Yang, J.-H.; Xu, P. Hf isotopic compositions of the standard zircons and baddeleyites used in U–Pb geochronology. *Chem. Geol.* **2006**, *234*, 105–126.
49. Lu, Y.F. Geokit—A geochemical toolkit for Microsoft Excel. *Geochimica* **2004**, *33*, 459–464.
50. Middlemost, E.A. Naming materials in the magma/igneous rock system. *Earth Sci. Rev.* **1994**, *37*, 215–224.
51. Winchester, J.; Floyd, P. Geochemical discrimination of different magma series and their differentiation products using immobile elements. *Chem. Geol.* **1977**, *20*, 325–343.
52. Pearce, J.A. Trace element characteristics of lavas from destructive plate boundaries. *Andesites* **1982**, *8*, 525–548.
53. Coleman, R.G.; Engelhardt, W. *What Is an Ophiolite?*; Springer Science and Business Media LLC: Berlin/Heidelberg, Germany, 1977; pp. 1–7.
54. Taylor, S.R.; McLennan, S.M. *The Continental Crust: Its Composition and Evolution*; Blackwell: Oxford, UK, 1985.
55. Sun, S.S.; McDonough, W.F. Chemical and isotopic systematics of oceanic basalts: Implications for mantle composition and processes. *Geol. Soc. London Spéc. Publ.* **1989**, *42*, 313–345.
56. Niu, Y.; O'Hara, M.J. Origin of ocean island basalts: A new perspective from petrology, geochemistry, and mineral physics considerations. *J. Geophys. Res. Space Phys.* **2003**, *108*, B4.
57. Liu, B., Ma, C., Zhang, J., Xiong, F., Huang, J. and Jiang, H. Petrogenesis of Early Devonian intrusive rocks in the east part of Eastern Kunlun Orogen and implication for Early Palaeozoic orogenic processes. *Acta Petrol. Sin.* **2012**, *28*, 1785–1807.
58. Belousova, E.A.; Griffin, W.L.; Pearson, N.J. Trace element composition and cathodoluminescence properties of southern African kimberlitic zircons. *Miner. Mag.* **1998**, *62*, 355–366.

59. Belousova, E.A.; Griffin, W.L.; O'Reilly, S.Y. Zircon Crystal Morphology, Trace Element Signatures and Hf Isotope Composition as a Tool for Petrogenetic Modelling: Examples from Eastern Australian Granitoids. *J. Pet.* **2005**, *47*, 329–353.
60. Belousova, E.A.; Griffin, W.L.; O'Reilly, S.Y.; Fisher, N. Igneous zircon: Trace element composition as an indicator of source rock type. *Contrib. Miner. Pet.* **2002**, *143*, 602–622.
61. Kirkland, C.L.; Smithies, R.; Taylor, R.; Evans, N.; McDonald, B. Zircon Th/U ratios in magmatic environs. *Lithos* **2015**, *212*, 397–414.
62. Stacey, J.S. and J.D. Kramers, Approximation of terrestrial lead isotope evolution by a two-stage model. *Earth Planet. Sci. Lett.* **1975**. 26, 207–221.
63. Wu, F.Y., Li, X.H., Zheng, Y.F. and Gao, S. Lu-Hf isotopic systematics and their applications in petrology. *Acta Petrol. Sin.* **2007**, *23*, 185–220.
64. Xu, J., Zhou, W., Zhao, X., Wang, B., Li, H., Chang, F. and XinBiao, L. Zircon U-Pb age and Hf isotopic characteristics of the Neoproterozoic globular granitic gneiss in Nomuhong area, east Kunlun. *Miner. Explor.* **2020**, *11*, 1–9.
65. Graham, I.; Cole, J.; Briggs, R.; Gamble, J.; Smith, I.E.M. Petrology and petrogenesis of volcanic rocks from the Taupo Volcanic Zone: A review. *J. Volcanol. Geotherm. Res.* **1995**, *68*, 59–87.
66. Morra, V.; Secchi, F.; Melluso, L.; Franciosi, L. High-Mg subduction-related Tertiary basalts in Sardinia, Italy. *Lithos* **1997**, *40*, 69–91.
67. Naumann, T.R.; Geist, D.J. Generation of alkalic basalt by crystal fractionation of tholeiitic magma. *Geol.* **1999**, *27*, 423.
68. Dessureau, G.; Piper, D.J.; Pe-Piper, G. Geochemical evolution of earliest Carboniferous continental tholeiitic basalts along a crustal-scale shear zone, southwestern Maritimes basin, eastern Canada1Geological Survey of Canada contribution, 1999035.1. *Lithos* **2000**, *50*, 27–50.
69. DePaolo, D.J. Trace element and isotopic effects of combined wallrock assimilation and fractional crystallization. *Earth Planet. Sci. Lett.* **1981**, *53*, 189–202.
70. Halama, R.; Marks, M.; Brügmann, G.; Siebel, W.; Wenzel, T.; Markl, G. Crustal contamination of mafic magmas: Evidence from a petrological, geochemical and Sr–Nd–Os–O isotopic study of the Proterozoic Isortoq dike swarm, South Greenland. *Lithos* **2004**, *74*, 199–232.
71. Mir, A.R.; Alvi, S.H.; Balaram, V. Geochemistry of the mafic dykes in parts of the Singhbhum granitoid complex: Petrogenesis and tectonic setting. *Arab. J. Geosci.* **2010**, *4*, 933–943.
72. Zhao, J.H.; Zhou, M.F. Geochemistry of Neoproterozoic mafic intrusions in the Panzhihua district (Sichuan Province, SW China): Implications for subduction-related metasomatism in the upper mantle. *Precambrian Res.* **2007**, *152*, 27–47.
73. Sklyarov, E.V.; Gladkochub, D.; Mazukabzov, A.; Menshagin, Y.; Watanabe, T.; Pisarevsky, S. Neoproterozoic mafic dike swarms of the Sharyzhalgai metamorphic massif, southern Siberian craton. *Precambrian Res.* **2003**, *122*, 359–376.
74. McKenzie, D.; Bickle, M.J. The Volume and Composition of Melt Generated by Extension of the Lithosphere. *J. Pet.* **1988**, *29*, 625–679.
75. Wang, K.; Plank, T.; Walker, J.D.; Smith, E.I. A mantle melting profile across the Basin and Range, SW USA. *J. Geophys. Res. Space Phys.* **2002**, *107*, ECV 5.
76. Pearce, J.A.; Peate, D.W. Tectonic implications of the composition of volcanic arc magmas. *Annu. Rev. Earth Planet Sci.* **1995**, *23*, 251–285.
77. Sajona, F.G.; Maury, R.C.; Pubellier, M.; Leterrier, J.; Bellon, H.; Cotten, J. Magmatic source enrichment by slab-derived melts in a young post-collision setting, central Mindanao (Philippines). *Lithos* **2000**, *54*, 173–206.
78. Hanyu, T.; Tatsumi, Y.; Nakai, S.; Chang, Q.; Miyazaki, T.; Sato, K.; Tani, K.; Shibata, T.; Yoshida, T. Contribution of slab melting and slab dehydration to magmatism in the NE Japan arc for the last 25 Myr: Constraints from geochemistry. *Geochem. Geophys. Geosyst.* **2006**, *7*, doi:10.1029/2005GC001220.
79. Tian, L.; Castillo, P.R.; Hilton, D.R.; Hawkins, J.W.; Hanan, B.B.; Pietruszka, A.J. Major and trace element and Sr-Nd isotope signatures of the northern Lau Basin lavas: Implications for the composition and dynamics of the back-arc basin mantle. *J. Geophys. Res. Space Phys.* **2011**, *116*, 11.
80. Wang, Q.; Zhao, Z.; Bai, Z.; Bao, Z.; Xiong, X.; Mei, H.; Xu, J.; Wang, Y. Carboniferous adakites and Nb-enriched arc basaltic rocks association in the Alataw Mountains, north Xinjiang: Interactions between slab melt and mantle peridotite and implications for crustal growth. *Chin. Sci. Bull.* **2003**, *48*, 2108–2115.

81. Woodhead, J.; Hergt, J.M.; Davidson, J.; Eggins, S. Hafnium isotope evidence for 'conservative' element mobility during subduction zone processes. *Earth Planet. Sci. Lett.* **2001**, *192*, 331–346.
82. Woodhead, J.; Eggins, S.; Johnson, R. Magma genesis in the New Britain island arc: Further insights into melting and mass transfer processes. *J. Petrol*. **1998**, *39*, 1641–1668.
83. Pearce, J.A. Geochemical fingerprinting of oceanic basalts with applications to ophiolite classification and the search for Archean oceanic crust. *Lithos* **2008**, *100*, 14–48.
84. Feng, J., Pei, X., Yu, S., Ding, S., Li, R., Sun, Y., Zhang, Y., Li, Z., Chen, Y. and Zhang, X. The discovery of the mafic-ultramafic melange in Kekesha area of Dulan County, East Kunlun region, and its LA-ICP-MS zircon U-Pb age. *Geol. China* **2010**, *37*, 28–38.
85. Li, C.F.; Li, X.H.; Li, Q.L.; Guo, J.H.; Li, X.H.; Yang, Y.H. Rapid and precise determination of Sr and Nd isotopic ratios in geological samples from the same filament loading by thermal ionization mass spectrometry employing a single-step separation scheme. *Anal. Chim. Acta* **2012**, *727*, 54–60.
86. Wang, Y.C.; Sun, F.Y. The Middle–Late Silurian granitoids in the Eastern Kunlun Orogenic Belt, NW China: Petrogenesis and implications for tectonic evolution. *Arab. J. Geosci.* **2019**, *12*, 568.
87. Zhao, Z., Ma, H., Wang, B., Bai, Y., Li, R. and Ji, W. The evidence of intrusive rocks about collision-orogeny during Early Devonian in Eastern Kunlun area. *Geol. Rev*. **2008**, *54*, 47–56.
88. Ren, J., Liu, Y., Feng, Q., Han, W., Gao, H. and Zhou, D. LA-ICP-MS U-Pb Zircon Dating and Geochemical Characteristics of Diabase-Dykes from the Qingshuiquan Area, Eastern Kunlun Orogenic Belt. *Acta Petrol. Sin*. **2009**, *25*, 1135–1145.
89. Gao, F.X.; Xiao, P.X.; Xie, C.R. Zircon LA-ICP-MS U-Pb dating and geological significance of Bashierxi granite in the eastern Kunlun area, China. *Geol. Bull. China* **2010**, *29*, 1001–1008.
90. Wang, X.X., Hu, N.G., Wang, T., Sun, Y.G. and Qi, Q.J. Late Ordovician Wanbaogou granitoid pluton from the southern margin of the Qaidam basin: Zircon SHRIMP U-Pb age, Hf isotope and geochemistry. *Acta Petrol. Sin.* **2012**, *28*, 2950–2962.
91. Wang, Y.; Zhang, A.; Fan, W.; Zhang, Y.; Zhang, Y. Origin of paleosubduction-modified mantle for Silurian gabbro in the Cathaysia Block: Geochronological and geochemical evidence. *Lithos* **2013**, *160*, 37–54.
92. El Aouli, E.H.; Gasquet, D.; Cheilletz, A. Lower Cryogenian calc-alkaline mafic rocks of the Western Anti-Atlas (Morocco): An example of orogenic-like magmatism in an extensional setting. *J. Afr. Earth Sci.* **2010**, *58*, 81–88.
93. Chen, N.; Sun, M.; Zhang, K.; Zhu, Y. 40Ar-39Ar and U-Pb ages of metadiorite from the East Kunlun Orogenic Belt: Evidence for Early-Paleozoic magmatic zone and excess argon in amphibole minerals. *Chin. Sci. Bull.* **2001**, *46*, 330–333.
94. Zhang, Z.; Li, K.; Li, J.; Tang, W.; Chen, Y.; Luo, Z. Geochronology and geochemistry of the Eastern Erenhot ophiolitic complex: Implications for the tectonic evolution of the Inner Mongolia–Daxinganling Orogenic Belt. *J. Asian Earth Sci.* **2015**, *97*, 279–293.
95. Chen, N.; Sun, M.; Wang, Q.; Zhang, K.; Wan, Y.; Chen, H. U-Pb dating of zircon from the Central Zone of the East Kunlun Orogen and its implications for tectonic evolution. *Sci. China Ser. D Earth Sci.* **2008**, *51*, 929–938.
96. Zhou, Z.Q., Gao, X.D., Hu, Y.X. and Zhao, J. Early Palaeozoic stratigraphy and sedimentary-tectonic evolution in eastern Qilian Mountains, China. *Northwest Geosci*. **1996**, *17*, 1–58.
97. Tseng, C.Y.; Yang, H.J.; Yang, H.Y.; Liu, D.; Wu, C.; Cheng, C.K.; Chen, C.H.; Ker, C.M. Continuity of the North Qilian and North Qinling orogenic belts, Central Orogenic System of China: Evidence from newly discovered Paleozoic adakitic rocks. *Gondwana Res.* **2009**, *16*, 285–293.